# Analysis of Three-Dimensional Ciliary Beating by Means of High-Speed Stereomicroscopy

Peter F. M. Teunis and H. Machemer
Arbeitsgruppe Zelluläre Erregungsphysiologie, Ruhr-Universität Bochum, ND 6/28, Postfach 102148, D-44780 Bochum, Germany

ABSTRACT Results are presented on the analysis of three-dimensional motion of compound cilia or cirri in voltage-clamped specimens of the protozoan *Stylonychia mytilus*. Time series of three-dimensional data were obtained by using the anaxial illumination method for simultaneous recording of stereoscopic video images.

Data processing involved the following steps: determination of a reference coordinate system based solely on features present in each stereo-pair; tracing of cirral axes in digitized images, conversion to parameter curves by means of least-squares polynomial approximation, conversion of pairs of two-dimensional data to a series of three-dimensional data; correction for distortion due to projective shortening and conversion to a series of polynomial triplets, and analysis of the periodical components of the motion pattern in the frequency domain.

Reconstructed beating cycles show typical differences between hyperpolarization-induced ciliary activity and depolarization-induced ciliary activity. Reconstructions of the motion of the basal segment of a cirrus are in agreement with existing data. Analysis of the curvature and torsion of a cirral axis during beating does not reveal any simple pattern of propagated activity within the axoneme.

The return stroke may be subdivided into two phases. First, a curvature peak develops proximally. Secondly, a region with increased torsion arises more distally and spreads out in proximal direction. Both curvature and torsion return to minimal values by the beginning of the power stroke.

## INTRODUCTION

The study of ciliary and flagellar motion depends on the establishment of experimental data, which are in general not easy to obtain. In the first place, the caliber of the organelles approaches the resolution limit of the light microscope. Secondly, beating takes place at rather high speeds; an entire cycle takes some tens of milliseconds to be completed. This means that recording of successive frames has to be performed at high rates to obtain sufficiently detailed time information. Thirdly, ciliary (and flagellar) motion normally is three-dimensional (3D). This implies that a classical light-microscopic projection provides insufficient information about the cirral trajectory.

The frontal cirri of hypotrich ciliates consist of up to 75 cilia (or even more, in large species), densely packed together. A cirrus tapers toward the tip because posterior cilia are shorter; its extreme distal end is splayed (Machemer and Deitmer, 1987). The cirrus can be considered a compound structure of numerous integral cilia. Compared with a single cilium, the large size of a cirrus makes it easier to study, whereas synchronization of the component cilia preserves their individual behavior.

Two approaches have been used for the registration of ciliary movements: stroboscopic sampling of a stereotyped beating pattern, and direct high-speed recording. Real-time recording with a high-speed camera (Baba and Hiramoto, 1970) is preferential given that detailed knowledge about temporal events in ciliary beating is unavailable. Sleigh (1968) has documented a number of ciliary and flagellar beating types using conventional microcinematography. This approach is satisfactory for 2D beating (Blake, 1972; Blake and Sleigh, 1974). For 3D forms of beating, e.g., in lamellibranch lateral cilia *Paramecium*, and the majority of cirri in the hypotrich ciliate *Stylonychia*, the information remains incomplete.

Studies on the 3D geometry of beating flagella in sperm cells were performed by Woolley (Woolley, 1981; Woolley and Osborn, 1984). These were single exposures, however; the development in time of flagellar bends still remains obscure. In our laboratory, a dynamic adaptation of the tilted stage method for stereomicroscopy has been used to reconstruct cirral motion (Mogami et al., 1992). This method involves demanding experimental procedures, and the separation in time of the two sequential recording series produces errors which are hard to control.

Here we present the first results of 3D reconstructions of cirral movement based on high-speed video recordings of simultaneously displayed stereo-pairs. This paper deals with the mathematical procedures for transforming video data (as a sequence of stereo-pairs) to an analytical description of a beating pattern, in a form best suited for biomechanical analysis. Our aim is to provide a detailed geometrical description that may then serve as a basis for testing models of axonemal functioning.

## METHODS

### Video registration

Microscopic methods which image the phase properties of an object can be used to visualize cilia and flagella, as these organelles are densely packed

*Received for publication 21 December 1993 and in final form 14 April 1994.*

Address reprint requests to Dr. Teunis at his present address, National Institute of Public Health and Environmental Protection, Laboratory of Water and Food Microbiology, Anthonie van Leeuwenhoeklaan 9, P.O. Box 1, NL-3720 BA Bilthoven, The Netherlands.



0006-3495/94/07/381/14 $2.00

with filamentous structures. Methods such as differential interference contrast and, even more, Zernike phase contrast, produce good contrast with ciliary organelles, but both methods suffer from glare due to birefringence caused by the high degree of anisotropy within these organelles. With anaxial illumination, the influence of birefringence is much reduced, whereas the contrast remains fairly good (Teunis et al., 1992). Compared with differential interference contrast, anaxial illumination provides relatively thick optical sections. For our present goal this is an advantage. To keep track of the ciliary organelle during the whole beating cycle a rather large volume has to be observed (up to 100 $\mu$m in each direction). The use of small illumination apertures positioned laterally in the objective aperture has been reported to allow visual tracking of a cirrus throughout its beating cycle (Teunis et al., 1992).

We have equipped a standard research microscope with anaxial illumination by using small circular illumination apertures positioned laterally in the aperture plane. When the illumination aperture is displaced horizontally the image is shifted because of tilting of the optical axis of the microscope. This feature can be used to obtain stereomicroscopy at high magnifications in the normal microscope with a single objective. Near the objective back focal plane an image-doubling prism (Wolf, 1989) was positioned, resulting in the projection of two images adjacent to each other. L-shaped double polarizers such as those used in a stereoscopic slide projector were placed near the aperture plane and at a conjugate plane in the projection lens of the video camera. These polarizers enabled the selection of the appropriate partial image for the left and right parts of the double video image (the result can be seen in Fig. 1).

A stereoscopic registration method based on the device described above was used to obtain high-resolution space and time video recordings of simultaneous stereo-pairs. The microscopic setup allowed the use of a fairly large disparity angle ($\approx$25°) between partial images. A detailed description of the optical setup has been published elsewhere (Teunis et al., 1992).

Recordings were made on a high-speed recorder (MHS-200, NAC, Tokyo, Japan) at 200 fields/s. This recording rate is in fact still rather slow for the processes we are studying. In previous experiments high-speed cinematography was used to yield recordings at 250 frames/s (Baba and Hiramoto, 1970; Machemer and de Peyer, 1982; Sugino and Machemer, 1988). A simple addition allows us to reach a recording rate that exceeds the maximal speed of these classical experiments without the expense of an even faster video system. By flashing the strobe illumination twice during each video field, we obtain double exposures. The relatively long integration time of the Plumbicon camera tube allows for such a procedure. The result of such a double exposure is an image in which only the fast-moving parts are doubled, whereas the cell body, for instance, is merely imaged more brightly. The exact timing of the electronic flashes can be determined by observing the pulse artifacts in the video image (Fig. 1). In principle, the application of three or even more superimposed images would be possible, but the reduced contrast in the fast-moving cirri (i.e., those details illuminated only by a single flash) limits the use of this technique to two flashes/video field. We were thus able to record cirral movements with an effective rate of 400 images/s.

For an experiment, a cell was voltage-clamped under zero-current conditions (Machemer and Deitmer, 1987) at the resting potential. At this membrane voltage, the frontal cirri are quiescent (de Peyer and Machemer, 1978; Deitmer et al., 1984). The response to a series of depolarizing or hyperpolarizing voltage steps was recorded according to previously applied methods (de Peyer and Machemer, 1982a, b).

## Tracing of the stereographs

The video images were digitized on an image processor (DVS-3000, Hamamatsu Photonics K.K., Hamamatsu City, Japan ) connected to a personal computer (IEEE-488 interface). Irregularities in illumination, combined with the complexity of the images, precluded automated tracing of the cirral positions (see Discussion). As discussed in Teunis et al. (1992), the small effective illumination aperture causes the contrast of the imaged cirrus to change with its axial position. As a result, determination of the outline of this organelle often turned out to be difficult. Therefore, we used a computer-mouse-controlled cursor to trace manually the main axis of imaged cirri, both on the video screen and on the computer display. With the help of this device a number of positions along the axis of a frontal cirrus were determined (4 to 5 up to 128, depending upon the direction of the axis), and the coordinates were saved as a list of $(x, y)$ pairs for each partial image (Fig. 1).

When the axis of displacement of the double-illumination aperture and the prism base in the image-doubling device are not exactly perpendicular, the whole image is rotated a few degrees. If this occurs, the result is a minor mismatch between the coordinates of the left and right partial images. Ideally, there would be no vertical disparity between the left and right partial images. Any vertical disparity between coordinate points (persistent after visual alignment) was minimized by applying a rotation matrix, rotating over an angle, determined by least-squares minimization of the vertical disparity between both partial images.

The coefficients of a $4 \times 3$ matrix for transformation of the left and right 2D coordinates in the stereo-pair to 3D coordinates have been calculated previously (Teunis et al., 1992). Thus, we have to determine the coordinates of the objects we want to study in both partial images, and transform these to an appropriate set of 3D coordinates.

## Polynomial fit within a time slice

A cirral axis may be thought of as a list of points in space, each representing a position on this axis. In reality, however, the cirral axis is a spatial curve, i.e., a more or less smooth trajectory in space. When we want to analyze the shape of this curve a description as a list of vertex points is not very convenient. When, for instance, spatial derivatives are to be determined, approximation to some continuous function is required. A convenient way to describe a spatial curve is in the form of a set of three parameter functions.

For a start, left and right data were arranged as a set:

$$\{x_L(s), y_L(s), x_R(s), y_R(s)\}$$

with $s$ denoting the common parameter, which at this stage is the rank number of tracked data points.

The dissimilarities between scanned traces in the left and right partial images present a problem. First, projective shortening generally differs in both views. Secondly, the speed with which the tracking device is moved is not constant because we trace by hand. During fast movements the sampling rate may become a limiting factor, thereby generating varying numbers of samples in corresponding sections of cirral traces. (In addition to this, the end points of the left and right partial images of the axis may not be found at the correct position. Handling of errors introduced by such a mismatch are discussed in the section under Feature Extraction.)

The stereoscopic base is aligned with the $x$ axis so that the $y$ coordinate of both partial images must span an equal path. With this in mind, the correction for unequal scanning and projection of the $x$ coordinate was performed as follows: A polynomial was fitted to the $y_L(s)$ and $y_R(s)$ data, using least-squares approximation methods. Successive approximations with increasing order $N$ were calculated. The goodness of fit was judged by means of a $\chi^2$ criterion (Press et al., 1989). See the left part of Fig. 2 for a typical set of polynomial coefficients. Then a (polynomial) function was calculated, which maps $y_R(s)$ onto $y_L(s)$. With this affine transformation function, $x_R(s)$ was transformed so that now both scans were based on an identical parameter scale. Finally, polynomials were fitted to both $x$ traces to allow the use of a unified scale for $s$, the running parameter.

After this the 3D positions were calculated, applying the conversion matrix supplied in Teunis et al. (1992). As a result, the data are available in the form:

$$\{x(s), y(s), z(s)\}$$

with $s$ denoting the common parameter, now as a continuous variable over the range of the approximated curves.

At this point, a second affine transformation was performed correcting for projective deformation so that the parameter $s$ reflects the true distance along the cirral axis. This is convenient in view of subsequent use of the data for the calculation of geometric characteristics like curvature, torsion, etc.

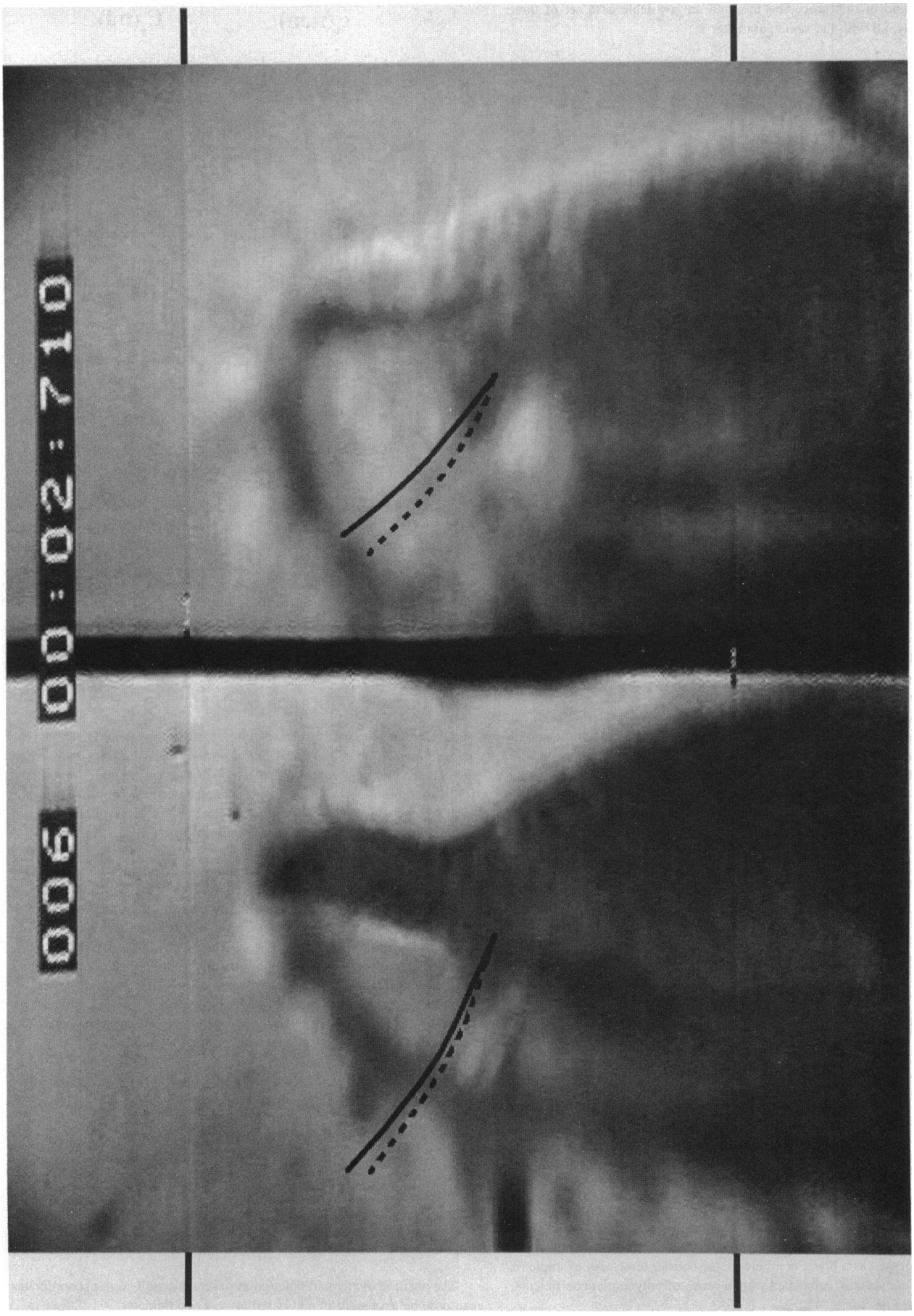


FIGURE 1 Example from a stereoscopic video registration of a voltage-clamped cell (anterior end up, see Fig. 3). The axis of the F2 cirrus is drawn in both partial images. The *solid curve* shows its position at the first flash, the *dashed line* shows the second position, 2.5 ms later (width of a partial image 180 μm). Note the two horizontal lines at about 1/5 and 4/5 of the height of the image: these are artifacts generated by the pulse which drives the strobe illumination.

At the end of this procedure the data are available as a set of three polynomials, all with the same parameter $s$:

$$x(s, m) = \sum_{n=0}^{N} c_x(n, m) \times s^n$$

$$y(s, m) = \sum_{n=0}^{N} c_y(n, m) \times s^n$$

$$z(s, m) = \sum_{n=0}^{N} c_z(n, m) \times s^n$$

Here, $x(s, m)$, $y(s, m)$, and $z(s, m)$ are the three spatial coordinates in a Cartesian system, described as polynomials of order $N$ with coefficients $c_x$, $c_y$, and $c_z$. The path length along the spatial curve is denoted $s$; $m$ is the rank number in the temporal sequence of sampled cirral axes (see Fig. 2 for an example).

To summarize, we use polynomials to represent cirral axes in space to: smooth fluctuations (tracing errors, digitization steps); achieve data compression; and convert data to a suitable form for further analysis (e.g., procedures involving differential geometry).

## Fourier analysis of temporal patterns

So far, we have restricted our analysis to single frames, i.e., stills of the cirral movement pattern. In our setup a frame consisted of a single video field taken every 5 ms representing two subsequent exposures superimposed as described in the section under Video Registration. Thus, we have a time series with equidistant data samples, 2.5 ms apart.

We are mainly interested in repetitive beating patterns; conversion to the frequency domain enables us to separate nonperiodic responses (inclination, see, e.g., de Peyer and Machemer, 1982a, b) from periodical beating. Furthermore, errors due to inaccurate tracking as well as those resulting from digitization may be removed by means of filtering (see also Blake, 1972). Finally, description in terms of a Fourier series provides data in a convenient form for further analysis, e.g., taking derivatives with respect to time as will be discussed under "Beating cones."

The polynomial coefficients $c_x(n, m)$, $c_y(n, m)$, and $c_z(n, m)$ can now be expressed as a Fourier series:

$$c_x(n, m) = \frac{1}{\sqrt{M}} \sum_{l=0}^{M-1} C_x(n, l) E^{-2\pi i l n/M}$$

$$c_y(n, m) = \frac{1}{\sqrt{M}} \sum_{l=0}^{M-1} C_y(n, l) e^{-2\pi i l n/M}$$

$$c_z(n, m) = \frac{1}{\sqrt{M}} \sum_{l=0}^{M-1} C_z(n, l) e^{-2\pi i l n/M}$$

The Fourier coefficients are calculated:

$$C_x(n, l) = \frac{1}{\sqrt{M}} \sum_{m=0}^{M-1} c_x(n, m) e^{2\pi i l m/M}$$

$$C_y(n, l) = \frac{1}{\sqrt{M}} \sum_{m=0}^{M-1} c_y(n, m) e^{2\pi i l m/M}$$

$$C_z(n, l) = \frac{1}{\sqrt{M}} \sum_{m=0}^{M-1} c_z(n, m) e^{2\pi i l m/M}$$

Hence, the complete set of polynomials for one Cartesian coordinate axis can be expressed as a linear combination of Fourier terms. An example of a set of power spectra, calculated from a series of polynomial coefficients, is shown in Fig. 2.

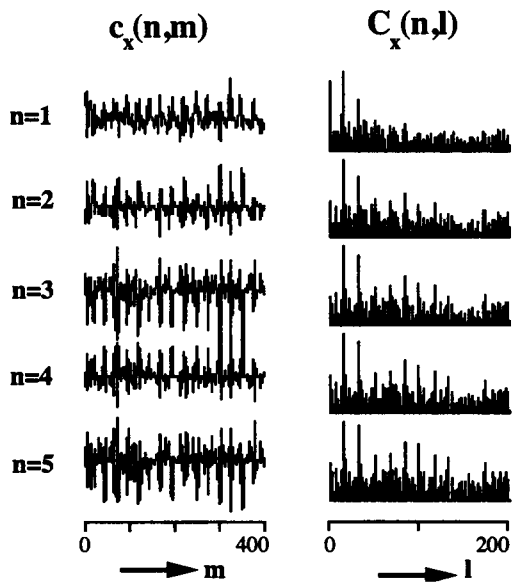


FIGURE 2 *Left*: Time series of polynomial coefficients (rank number m, 400 samples at 2.5 ms intervals, total observation time 1000 ms), for one complete trial. From the top down: $c_x(1, m)$ through $c_x(5, m)$, used to calculate positions on the cirral axis (parameter $s$): $x(s, m) = c_x(1, m)s + c_x(2, m)s^2 + c_x(3, m)s^3 + c_x(4, m)s^4 + c_x(5, m)s^5$. Only the $x$ set is shown, the $y$ and $z$ sets are similar. Vertical axes are scaled arbitrarily to the largest component to emphasize only the time dependence of the coefficients and not their absolute magnitudes. *Right*: Set of power spectra, obtained by Fourier transformation of the data shown left. Vertical axes are scaled arbitrarily to the largest component to show the frequency dependence of the coefficients.

## A cell-based reference system

Finally, we have to establish a reference coordinate system. Given that the anterior part of the cell is always in view and the positions of the cirri on the cell are fairly stereotypical, we use the bases of the three frontal cirri for the definition of the $(x, y)$ plane. This plane does not coincide with the "ventral" (substrate-oriented) surface of the cell; the anterior end of the cell is tilted upward, away from the substrate (Mogami et al., 1992).

To comply with existing definitions of the reference system (Mogami et al., 1992), we have chosen the direction of the positive $x$ −axis, −23° offset from the vector connecting the base of the F1 cirrus with the base of the F3 cirrus. In a right-hand coordinate system, this puts the positive $y$ axis approximately pointing anteriad along the longitudinal axis of the cell. In Fig. 3 the position of the reference system in the cell is illustrated.

For a description of cirral coordinates the origin of the reference system is translated to the base of the cirrus concerned. For instance, when we position the origin at the base of the F1 cirrus, the two vectors pointing at the bases of the two other cirri, $\mathbf{v}_2^2$ and $\mathbf{v}_3$, determine the $x$Oy plane. The three unit vectors of the reference coordinate system are then:

$$\mathbf{e}_z = \frac{\mathbf{v}_2 \times \mathbf{v}_3}{\sqrt{(\mathbf{v}_2 \times \mathbf{v}_3) \times (\mathbf{v}_2 \times \mathbf{v}_3)}},$$

$$\mathbf{e}_x = A\left(\frac{\mathbf{v}_3}{\sqrt{\mathbf{v}_3 \times \mathbf{v}_3}}\right), \qquad \mathbf{e}_y = -\mathbf{e}_x \times \mathbf{e}_z$$

with the rotation matrix $A$ defined as:

$$A = \begin{pmatrix} \cos\psi & \sin\psi & 0 \\ -\sin\psi & \cos\psi & 0 \\ 0 & 0 & 1 \end{pmatrix}, \qquad \psi = -23°$$

The position of any particular point in screen-based $(x, y, z)$ coordinates can now be expressed in cell-based $(x, y, z)$ coordinates.

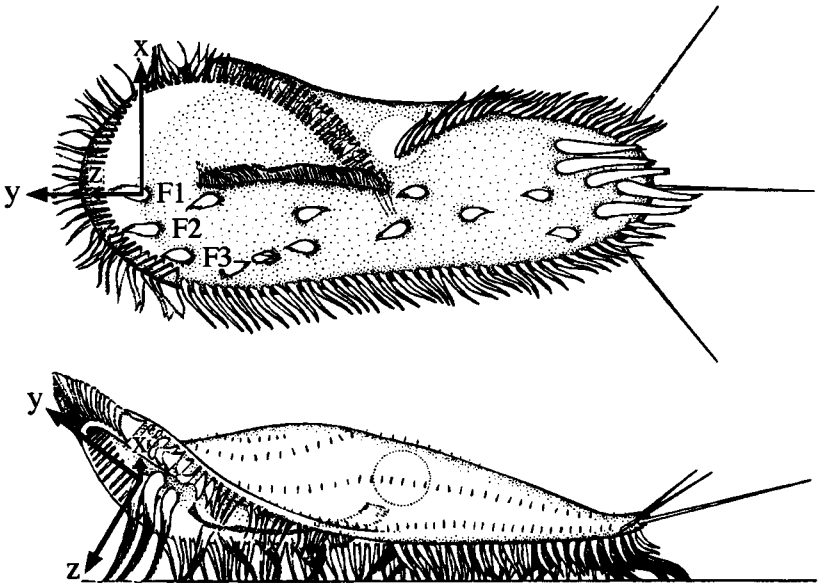


FIGURE 3 Reference coordinate system, as defined in the text, within a drawing of *S. mytilus* (original by Machemer and Machemer-Röhnisch). *Anterior end left, top*: oral side; *bottom*: left side; *F1–F3*: frontal cirri.

## RECONSTRUCTIONS

### Projections

Application of the procedures described above for the reconstruction of the movement pattern of a cirral axis produces a detailed series of spatial curves. Some examples are shown in Figs. 4–7 to illustrate the results obtained by our method. In the following examples, interpolation of Fourier coefficients (Oppenheim and Schafer, 1975) has been used to reconstruct axes at approximately 1-ms intervals to emphasize the temporal smoothness of the reconstruction.

In each of Figs. 4–7 a single reconstructed beating period was taken out of a large data set. Some of the cycles show discontinuity. This occurs when successive cycles in the reconstructed set are not exactly identical so that the beginning and the end of a cycle do not exactly match. For ease of comparison we have cyclically shifted the data so that all cycles start more or less at the same phase. The responses to depolarizing voltage steps (Figs. 4 and 5) start approximately at the beginning of the power stroke, the responses to hyperpolarizing voltage steps (Figs. 6 and 7) at the beginning of the return stroke. Positive directions of the (cell-based) reference axes are indicated. This means that in the *xy* projections (Figs. 4–7, *top*) the cell would be viewed from below (cirri facing the viewer) with anterior end pointing north; in *yz* projections (Figs. 4–7) the cell would be oriented upside-down (cirri up), with its anterior end eastward (to the right).

Comparison of the reconstructions in Figs. 4 and 5 on one hand and those in Figs. 6 and 7 on the other seems to

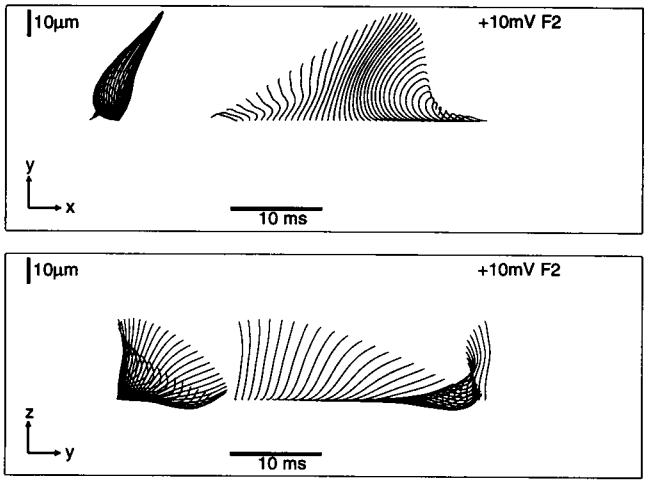


FIGURE 4 Projections of a reconstructed beating cycle of the F2 cirrus after a 10-mV depolarizing voltage step assembled from subsequent postures of the cirral axis. *Top*: Cell-based *xy* projection (axial view, anterior end pointing upward). *Bottom*: Cell-based *yz* projection (lateral view, anterior end pointing to the right). In the *leftmost* part of each figure all cirral axes have been drawn from the same starting point; on the *right*, the same data are shown with a small displacement after each time increment.

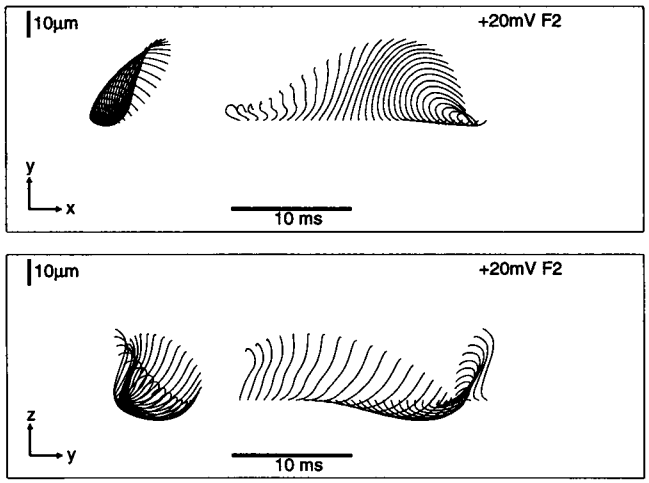


FIGURE 5 Projections of a reconstructed beating cycle of the F2 cirrus after a 20-mV depolarizing voltage step assembled from subsequent postures of the cirral axis. Viewing directions as described in Fig. 4. Note the longer time bar, indicating an increase in beating frequency.

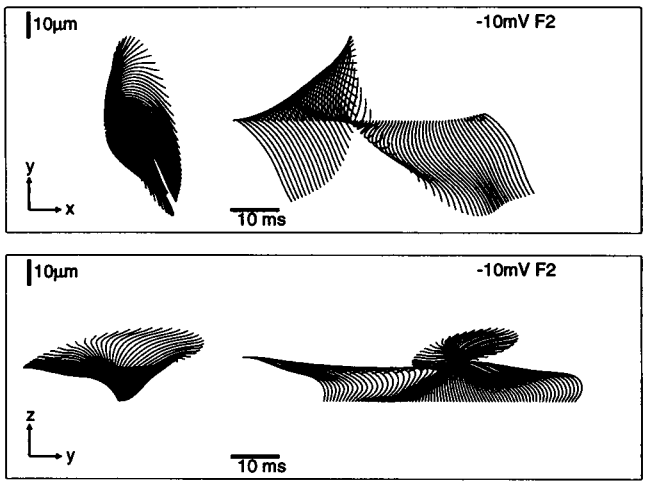


FIGURE 6 Projections of a reconstructed beating cycle of the F2 cirrus after a 10-mV hyperpolarizing voltage step assembled from subsequent postures of the cirral axis. *Top*: Cell-based *xy* projection (axial view, anterior end pointing upward). *Bottom*: Cell-based *yz* projection (lateral view, anterior end pointing to the right). In the *leftmost* part of the figures all cirral axes have been drawn from the same starting point; on the *right* the same data are shown, with a small displacement after each time increment.

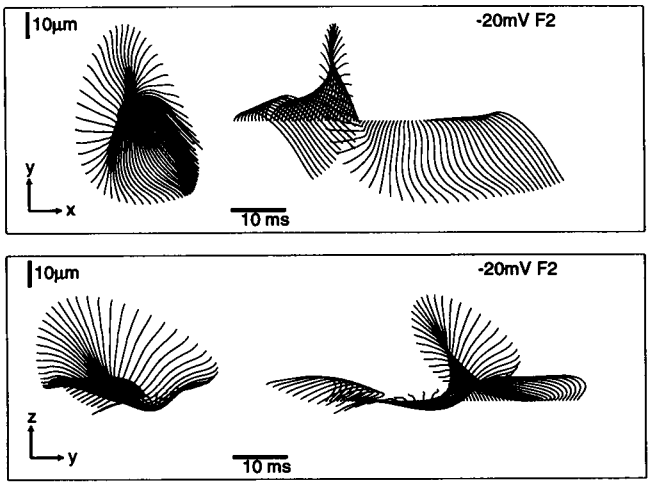


FIGURE 7 Projections of a reconstructed beating cycle of the F2 cirrus after a 20-mV hyperpolarizing voltage step assembled from subsequent postures of the cirral axis. Viewing directions as described in Fig. 6.

confirm the fundamental difference between so-called depolarization-induced ciliary activity (DCA) (de Peyer and Machemer, 1982a, b), and hyperpolarization-induced ciliary activity (HCA). The length of the 10-ms time bars indicates that in these samples the responses to depolarization occur with nearly twice as high a frequency as those to equally strong hyperpolarizations. The pattern that seems to emerge is that during hyperpolarization the cirrus covers a wider conical volume; the *xy* projection extends across both right-hand quadrants. The responses to stronger hyperpolarizations even indicate that all four quadrants are covered in this projection. All the depolarization-induced responses, on the other hand, are confined to the top right quadrant.

## Base angles

By taking into account only the first-order polynomial coefficients, the angular offset of the proximal part of the cirral

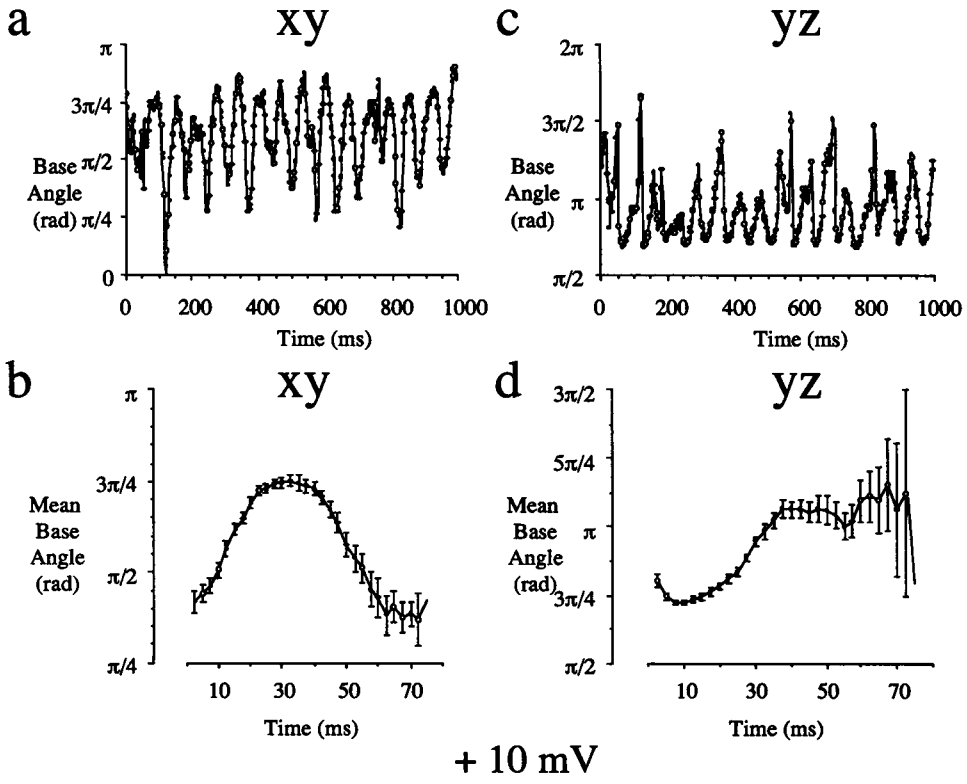


FIGURE 8 Base angle (angular deviation of the proximal part) of the cirral axis. Voltage step +10 mV, onset at 0 ms, duration 1000 ms. (*a*) projected on the cell-based *xy* plane, calculated over a complete trial (every 2.5 ms). (*b*) same projection as in (*a*), averaged data from the cycles 4–14. (*c*) projected on the cell-based *yz* plane, calculated over a complete trial (every 2.5 ms). (d) same projection as in (c), averaged data from the cycles 4–14. Vertical bars in b and d are standard errors.

axis from a reference coordinate, i.e., the base angle, can be easily calculated. In Fig. 8 the changes in base angle are shown, measured with respect to the positive $x$ axis after a depolarizing 10-mV voltage step. Fig. 8, *a* and *b*, show *xy* projections formerly referred to as axial views with respect to the ciliary base (Mogami and Machemer, 1991; Mogami et al., 1992; Sugino and Machemer, 1987). Both the complete data set (Fig. 8 *a*) and an averaged cycle extracted from these data (Fig. 8 *b*) are given. Averaging was performed by pooling samples that were one cycle apart, starting at an arbitrary point after completion of the first few, transient, cycles. Figs.8, *c* and *d* show the *yz* views for the same trial. This projection has been referred to as the lateral view (Mogami and Machemer, 1991; Mogami et al., 1992; Sugino and Machemer, 1987). Note that the fluctuations tend to increase toward the right part of the graphs. This is caused by averaging over a number of cycles of not exactly matching lengths (mean 72.0 ms, standard deviation 4.5 ms). The *xy* projection seems to indicate that there was not a large difference in timing between both parts of the cycle; back and forth movement involved approximately equal (though mirrored) slopes with time. The *yz* projection presents quite a different view, a comparatively slow, steady power stroke, followed by a more or less stationary phase, after which a fast return stroke completes the cycle.

Fig. 9 gives an example of the changes in base angle following a 10-mV hyperpolarizing voltage step. The data in these graphs were calculated from the coefficients in Fig.2. Shown are *xy* (Fig. 9, *a* and *b*), and *yz* projections (Fig. 9, *c* and *d*). At first sight the averaged axial (*xy*) view does not seem to represent the data in Fig. 9 *a* very well. When one keeps in mind, however, that the transition from $+\pi$ to $-\pi$ radians is in fact a continuous one, the differences are not so grave at all. The averaging procedure has merely smoothed the extreme angles to some extent. The beating cycle may be divided in two sections with different angular velocities representing power and return stroke (in this order, in Fig. 9 *b*). This bisection cannot be reproduced so easily in Fig. 9 *d*, possibly because the fast return stroke lies perpendicular to the plane of projection.

## Beating cones

The analysis in the preceding figures was based on apparent motion within projections under a few selected angles. Not only are such data difficult to interpret, they also only provide partial information about the motion we are trying to analyze. When the base angles could be visualized in three dimensions, the motion pattern might be easier to interpret.

Fig. 10 *a* shows a 3D view of the trajectory of the basal part of an F2 cirrus, after a 10-mV depolarizing voltage step. Projection is as if the cell were viewed more at its anterior right end. The beating cycle is drawn as a set of unit vectors, clearly showing the conical surface assumed by Sugino and Machemer (1987) to infer 3D motion parameters from 2D recordings. Each vector represents data from a single image; the time increment between successive positions equals 2.5 ms. Hence, the spacing of individual vectors indicates the speed of the basal segment during a beating cycle. In *Stylonychia*, the power stroke is slower than the return stroke. In Fig. 10 *a* the power stroke (~0 ms to ~30 ms) is directed

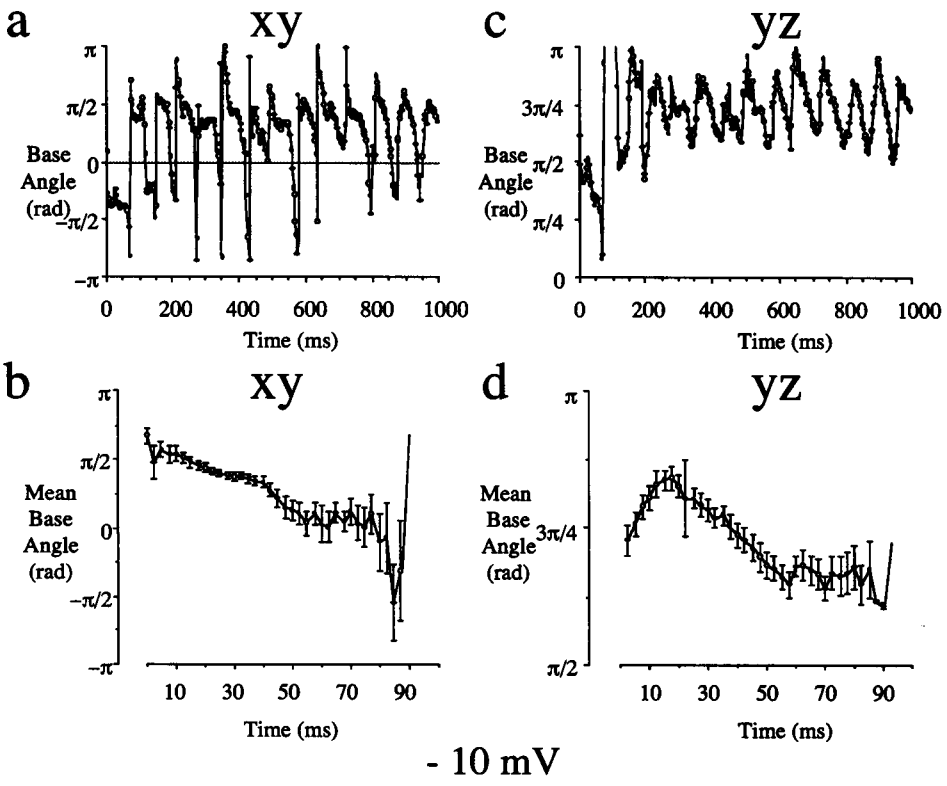


FIGURE 9 Base angle (angular deviation of the proximal part) of the cirral axis. Voltage step −10 mV, onset at 0 ms, duration 1000 ms. (*a*) projected on the cell-based *xy* plane, calculated over a complete trial (every 2.5 ms). (*b*) same projection as in (*a*), averaged data from the cycles 3–12. *c*: projected on the cell-based *yz* plane, calculated over a complete trial (every 2.5 ms). (*d*) same projection as in (*c*), averaged data from the cycles 3–12. Vertical bars in *b* and *d* are standard errors.

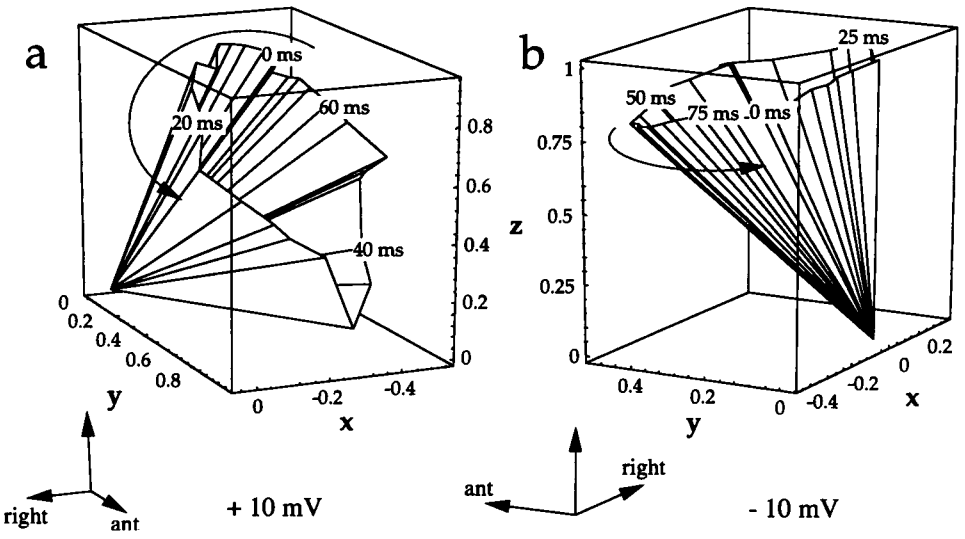


FIGURE 10 (*a*) Perspective view of the trajectory of the cirral base (the proximal part of the cirral axis), after a +10-mV depolarizing voltage step, as seen when watching at the anterior end of the cell (note direction of the positive *y* axis). Successive directions are plotted as unit vectors. Time ticks within cycle are given at 0, 20, 40 and 60 ms, starting approximately at the middle of the power stroke. (*b*) Perspective view of the trajectory of the cirral base after a −10-mV hyperpolarizing voltage step, as seen when looking from posterior left at the cell (note direction of the positive *y* axis). Time ticks within cycle are given at 0, 25, 50 and 75 ms, starting near the end of the power stroke.

toward the anterior left. Note that the return stroke is executed in the vicinity of the cell surface.

In Fig. 10 *b* the same is shown for the basal segment of an F2 cirrus during the response to a −10-mV hyperpolarizing voltage step. The cone is viewed from posterior and left to give a better insight into its orientation (note the directions of the reference axes). Here, the slower power stroke (~50 ms to ~0 ms) is directed toward the posterior right (cf. Fig. 6. Note the transient depression in speed during the return stroke (~47.5 ms).

## Angular velocity

As has been demonstrated above, the trajectory of the proximal segment of a beating cirrus can be determined unambiguously. As a consequence, it is also possible to calculate its angular velocity. This is a vectorial quantity, but for the moment we are not primarily concerned with the direction (the reader may infer the direction of the angular velocity from Figs. 10, *a* and *b*). The magnitude of the angular velocity during (approximately) one beating cycle after a depolarizing voltage step is given in Fig. 11 *a*. In Fig. 11 *b* the same is shown for the response to a hyperpolarizing voltage step. Obviously, the response to a depolarization occurs with a higher speed than that to a hyperpolarization of equal strength. Note, however, that the ratio of angular speeds is almost 2:1, whereas the ratio of the cycle lengths is significantly smaller (about 1.5:1). This is in agreement with Figs. 10, *a* and *b*, in which the cone described during depolarization is wider than that during hyperpolarization.

## Curvature

When we proceed further towards the extraction of parameters that might be relevant for axonemal sliding, analysis of the shape of the cirral axis in the course of a beating cycle is indispensable (Brokaw, 1971; Hines and Blum, 1978; Holwill et al., 1979). In Figs. 12 and 13 the curvature and torsion of the reconstructed axes are given both as a function of time ($t$), and distance ($s$) along the axoneme.

If the position vector $\mathbf{r}(s, t) = \{x(s, t), y(s, t), z(s, t)\}$, and a prime (l), denotes taking the derivative with respect to distance $s$, the curvature of a spatial curve is defined as:

$$\kappa = \frac{|\mathbf{r}' \times \mathbf{r}''|}{|\mathbf{r}'|^3}$$

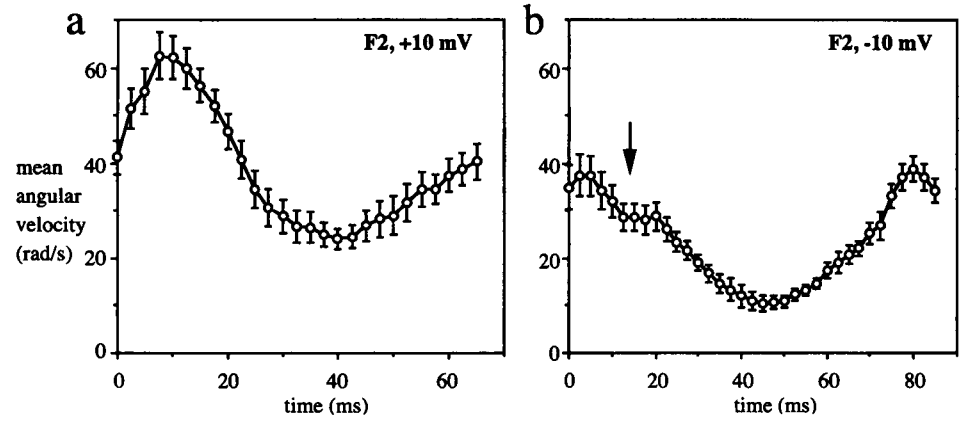


FIGURE 11 (*a*) Magnitude of the angular velocity of the proximal segment of cirrus F2 during a beating cycle, after a +10-mV depolarizing voltage step. Averaged data from eight successive cycles; vertical bars indicate standard errors. Time scale corresponds to that of the beating cone in Fig. 10 *a*. (*b*) Magnitude of the angular velocity of the proximal segment during a beating cycle, after a −10-mV hyperpolarizing voltage step. Arrow: discontinuity in angular velocity during power stroke. Averaged data from eight successive cycles; error bars indicate standard errors. Time scale corresponds to that of the beating cone in Fig. 10 *b*.

Torsion is defined as:

$$\tau = \frac{\left[\begin{vmatrix} x' & y' & z' \\ x'' & y'' & x'' \\ x''' & y''' & z''' \end{vmatrix}\right]}{|\mathbf{r}' \times \mathbf{r}''|^2}$$

We will confine ourselves here to providing the results of our calculations. For more information the reader is referred to a textbook on analytical geometry (Thomas and Finney, 1992).

Figs. 10 *a* and 12 are derived from the same set of data recorded in response to a +10-mV (depolarizing) voltage step with identical time scales. Small values of both $\kappa$ and $\tau$ during the power stroke indicate the largely straight state of the cirral axis during this part of the cycle. At the onset of the return stroke, a curvature peak develops near the cirral origin. This area of increased curvature does not move with time along the axis by a significant amount. Instead, shortly afterward, a zone of increased torsion develops, distal with respect to the area described above. Within this zone, a region of torsion with negative sign is followed by a region of positive torsion, with increasing $s$ (going in distal direction). In other words: a bending zone develops basally and then proceeds distally, in the meantime rotating about the axis. When time proceeds further, the region of positive torsion seems to move towards the cirral base until the maximum lies at about $s = 18$ $\mu$m (i.e., at about 30% of the length of the total axis, from the base); then the curve flattens out near the end of the return stroke. During this remaining part of the return stroke, the curvature remains low.

In Figs. 10 *b* and 13 the same data are shown for a −10-mV (hyperpolarizing) voltage step. Although the timing differs to some extent, a quite similar pattern to that shown in Figs. 10 *a* and 12 emerges. During the power stroke on which the axis is stretched, both curvature and torsion are small. The return stroke starts with the development of a region of increased curvature near the cirral base. With hyperpolarization, this region seems to lie slightly more distal than with depolarization. Here, too, a zone of increased torsion develops near the tip of the cirrus, and the position of the peak moves in basal direction as time proceeds toward the conclusion of the return stroke.

## DISCUSSION

### Stereo microscopy

We have demonstrated that high-speed stereomicroscopic registration methods enable studying the motion of a ciliary organelle in space, providing a so-far unequalled combination of temporal and spatial resolution. At the same time, the

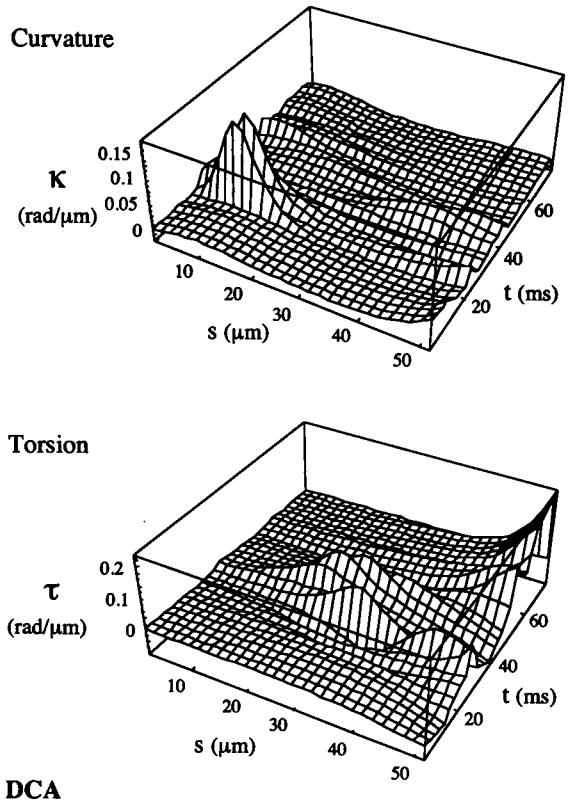


FIGURE 12 Curvature ($\kappa$) and torsion ($\tau$) of the cirral axis during a DCA beating cycle after a +10-mV depolarizing voltage step. Position on the axis measured as path length $s$ (see text for definitions). Time scale ($t$, in ms) as in Figs. 10 *a* and 11 *a*.

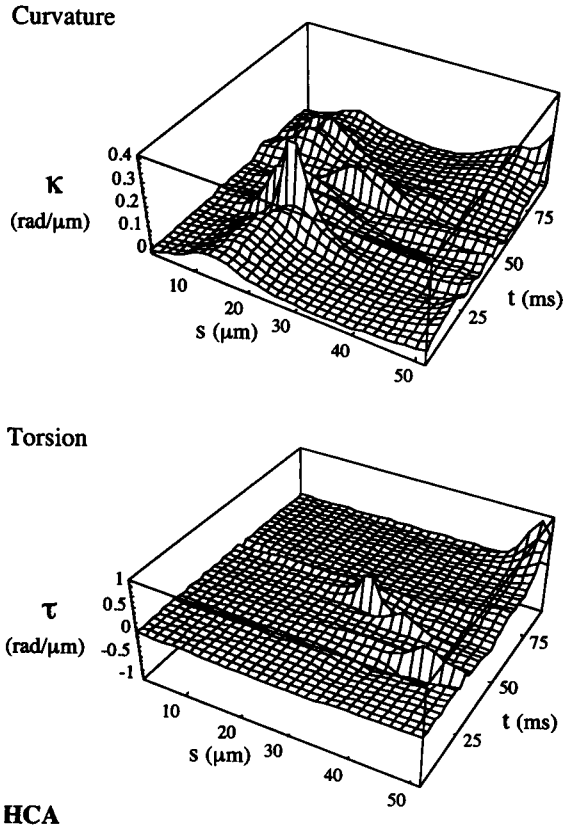


FIGURE 13 Curvature ($\kappa$) and torsion ($\tau$) of the cirral axis during an HCA beating cycle after a −10-mV hyperpolarizing voltage step. Position on the axis measured as path length $s$ (see text for definitions). Time scale ($t$, in ms) as in figs. 10 *b* and 11 *b*.

experimentalist is provided with the advantages of video registration as compared with the classical methods using cinematographic recording. The simultaneous registration of both partial images of the stereo pair preserves excellent temporal resolution at the expense of a small trade-off in spatial resolution. The video field has to be divided in two halves, but via adjustment of the magnification the loss of resolution can be compensated. These simultaneous stereographs are well suited for quantitative analysis, inasmuch as the viewer is provided instantaneous depth information with a constant angular disparity between the left and right partial images. This means that the conversion from left and right 2D images to a single 3D image remains exactly the same throughout an experimental session. The angular disparity is even independent of the chosen magnification: a change in objective lens does not alter its magnitude or direction, as long as the numeric aperture of the objective lens exceeds that of the illumination (Teunis et al., 1992).

All necessary information for the reconstruction of the 3D coordinates is present in every stereo-pair. This implies that, if the cell should shift its position during a recording session as may happen with strong stimulation, the accuracy of 3D reconstruction need not be affected. Since the reference system itself is based solely on features present in every image, even continuous recalibration during an experiment is possible.

## Feature extraction

The most delicate step in the analysis procedure is the tracing of cirral axes in the digitized video images. Attempts to use image-processing methods for the extraction of cirral outlines and/or axes are likely to fail because of the poor-quality images.

The angular disparity between the left and right partial image is such that the depth component, which has to be inferred from the spatial differences between these two partial images, can only be measured about 2.5 times as inaccurate as both lateral dimensions (Teunis et al., 1992). We have attempted to minimize the resulting errors by increasing the magnification as much as possible. Nevertheless, both $x$ coordinates include random fluctuations, and every fluctuation in the $x$ direction returns 2.5-fold in the derived $z$ value.

Because it is reasonable to assume that these fluctuations occur at random, a suitable smoothing procedure can diminish these tracing errors. In agreement with previous analyses of ciliary motility (Sugino and Machemer, 1988, 1990; Mogami et al., 1992), preliminary tests confirmed that the shapes to be analyzed would be smooth and of a rather simple geometry, i.e, having no sharp angles or complicated knots and usually bending in only one direction. Therefore, a least-squares approximation to polynomials of limited order will extract the most relevant information from manual tracing data.

The uncertainty in the traced cirral axes is especially significant when the distal ends are involved. When there is a large error in the coordinate of this end point, faulty conclusions may be drawn. In the case of discrepancy between image pairs, the length of the reconstructed axis will deviate from that of the other ones within the same sequence. If the error occurs between the left and right partial images of the same pair, correction for projective shortening will result in the calculation of an incorrect length and an incorrect direction of the distal end of the reconstructed cirral axis. The latter situation seems to be the most likely to occur, as it would involve only one incorrect trace. We have accounted for such errors in two ways. First, polynomial fitting in 3D enabled quick calculation of the length of the complete axis. If the lengths of the axes within a sequence fluctuated by more than 10%, these data were discarded. In some cases, retracing would produce better results (e.g., when only one or two axes were aberrant). In the second place, animated sequences of reconstructed axes could be viewed from any desired angle (cf. Figs. 4–7), thus providing the opportunity to detect any conspicuous movements pointing to bad tracing.

## Parametric description

When the shape of a cirral axis is to be studied in 3D, its description as a set of three polynomials with shared parameter $s$, equaling the path length along the curve, is quite beneficial. Investigation of the shape of the 3D curve requires the calculation of spatial derivatives. When all functions are expressed as parametrized polynomials, this reduces to an almost trivial task. Calculation of the curvature and torsion of a parametrized spatial curve on the basis of the description given above can thus be easily generalized. This is convenient in view of the processing of a large body of data with automated procedures.

As changes of shape with time are also to be investigated especially with respect to their periodic aspects, a description in terms of a Fourier series as discussed in Methods might be well suited. Obviously, the calculation of, e.g., temporal derivatives can be performed without much effort. The present results (Fig. 2) seem to indicate that cirral motion may include complex spectral contents: the movement of a cirral axis in time occurs in an essentially nonsinusoidal manner (Figs. 8 and 9).

When we take into account that there must be a limit to the speed at which these mechanical events take place, or that the changes in shape during beating are continuous functions of time, interpolation between the sampled data may be useful (Oppenheim and Schafer, 1975) in giving a detailed view of the cycle (Figs. 4–7). Of course, one must be very cautious with any conclusions about events occurring within a frequency band near the Nyquist limit (half of the sampling frequency). Here, doubling of the effective video field rate is quite beneficial because it rises the sample rate to a much safer value of 400 $s^{-1}$, yielding enough samples/beating cycle to achieve a good representation (Figs. 8 and 9).

## Reordering of sampled data

In previous studies on ciliary motion, a basic assumption has been that the beating cycle is highly stereotypical, the posture of the axis being always the same at corresponding phases of subsequent cycles. This is a necessary condition for the use of sorting methods which employ template matching (Mogami et al., 1992); axial and lateral projections are sorted according to their similarity to an arbitrary, normalized beating cycle. Normalization of the duration of a beating cycle seems to be a reasonable simplification. The duration of a cycle does not seem to change much over prolonged periods of stimulation (Fig. 2). According to Mogami et al. (1992), however, successive cycles do not always have exactly the same duration. Unfortunately, the magnitude of these fluctuations is not stated.

Nonetheless, (Mogami et al., 1992) abandoned the constant sampling rate and reordered the axial silhouettes entirely by their shapes. In the case of a variable beating period, mixing of data arisen under different hydrodynamical circumstances cannot be excluded. An additional error source may lie in the fact that sorting takes place in 2D projections where motion perpendicular to the viewing plane has few or ambiguous effects on the visible projection. Because of such "invisible" motion, erroneous sorting of projections is possible.

The method presented here provides sufficiently high sampling rates to enable analysis of the timing of events occurring within a single beating cycle (see, e.g., Figs. 8 and 9).

## Beating cones

Figs. 10 *a* and *b* are in agreement with the results of Sugino and Machemer (1987). These authors employed projections of the conical trajectory described by the basal part of the cirrus to estimate its spatial position and shape. Their approach produced correct results, but direct measurements of angular velocities are only possible when 3D data are used.

Because of the choices we have made for the method to describe our data sets as Fourier transformed polynomial coefficients, the calculations to arrive at these base angles are simpler than those used by Sugino and Machemer (1987), who take the direction of the line connecting the center of the cirral base with the cirral axis at a distance equal to the width of the cirrus at its base (Machemer and Sugino, 1986). With the present data, we merely take the first polynomial coefficient for each coordinate to obtain the direction of the tangent vector at the base.

A quick look at the reconstructions in Figs. 4–7 may suggest that the motion of the basal part contains but little information about the complete sequence of events within a beating cycle of the whole axoneme. There are, however, three important parameters involved here: 1) the width of the basal cone, 2) its orientation or inclination, and 3) the angular speed of the basal segment during a beating cycle.

The reconstructed beating cycles also suggest that the proximal segment of the cirrus pivots about its base, contrary to the observations of Sugino and Machemer (1990). However, the data presented here do not permit conclusions about whether the basal segment bends during beating or not. The viewing angle we have chosen provides a good overview of the cycle as a whole but not of the basal segment in particular. Only lateral viewing as employed by Mogami et al. (1992) and Sugino and Machemer (1988, 1990) enables direct observation of the most proximal part of the cirrus. The question of whether basal bending occurs has great bearing on the distribution of sliding over the axoneme. Since the occurrence of basal bending (and not pivoting) has been demonstrated convincingly in our laboratory, future modeling efforts may be directed at joining information on basal angles collected here with proximal bending at a small distance from a rigid cirral base.

In addition to the basal characteristics of cirral beating, we have analyzed the posture of the entire cirral axis by means of measuring its curvature. This will be described in the Cirral Shape section.

## Angular velocity

The changes in angular velocity during cirral beating show another difference between power stroke and return stroke. Both during depolarization and hyperpolarization, the power stroke is slower than the return stroke. This is a typical aspect of cirral beating in *Stylonychia* (Sleigh, 1968) as opposed to the beating cycle of *Paramecium*, where the return stroke constitutes the slowest part of the cycle. A slow power stroke might reflect a functional adaptation to "walking" locomotion on a substrate. It is conceivable that during contact with the substrate the velocity of the cirrus must be limited in order to retain sufficient friction within the contact area.

A second feature, which is still present after averaging over several cycles, is a minor discontinuity during the power stroke at hyperpolarized membrane voltages. This phenomenon was first described by Sleigh (1968) and confirmed later by Sugino and Machemer (1988). Cause and function of this phenomenon remain unknown.

## Cirral shape, as characterized by curvature and torsion

Standard measures developed for geometrical analysis of the curvature of a spatial trajectory have been applied to describe the shape of a beating cirrus. The curvature $\kappa$ can be thought of as the rate at which the normal plane (Definitions are based on a reference frame moving along the curve. This reference frame is built from three vectors: **T**, the unit tangential vector, **N**, the unit vector in the direction given by $d\mathbf{T}/ds$, and $\mathbf{B} = \mathbf{T} \times \mathbf{N}$, the binormal vector. Together, these three vectors make up the Frenet-frame. **B** and **T** define the so-called rectifying plane, B and N define the normal plane, and T and N define the osculating plane.) turns as a point moves along the curve (Thomas and Finney, 1992). Its inverse can be interpreted as a radius of curvature. The torsion or twist $\tau$ is

the rate at which the osculating plane twists about the direction of the tangent (**T**), as a point moves along the curve. The sign of $\tau$ is positive when the binormal vector **B** rotates in a right-hand fashion for a point traveling along the curve. The overall magnitude of curvature may also be expressed as a total curvature, $\lambda$:

$$\lambda = \sqrt{\kappa^2 + \tau^2}$$

In Figs. 12 and 13 it can be seen that peaks in $\kappa$ and $\tau$ do not coincide. This is confirmed when $\lambda$ is plotted in a similar fashion; the same peaks appear together in a single figure (not shown).

Analysis of ciliary beating in terms of curvature and torsion may enable increased precision in discrimination between the different phases of a beating cycle. Judged by these measures, three stages may be distinguished within a cycle: *1*) the power stroke, in which the axis is only weakly curved, and the angular speed is low; 2) the initial phase of the return stroke, in which a limited region near the base develops strong curvature (During this phase the angular speed is increased to a value twice or more of that during the power stroke); and 3) the final part of the return stroke, in which the curvature declines, and a twisted region develops distally.

Both with de- and hyperpolarization, the zone of increased torsion develops in a region with little curvature. As a result, this phenomenon may be of little significance with respect to the (generation of) shape of the cirral axis. Confrontation of the results from modeling studies with the present experimental data may enable more specific conclusions (see Appendix).

In the Beating Cones section, when the conical trajectory described by the basal segment of the cirral axis was discussed the question of basal pivoting or bending was addressed briefly. Independent observations have demonstrated that strong bending occurs at a very small distance from the base. As stated before, our observations did not include the most basal part of the cirrus. Therefore, the data presented here may be regarded as excluding this most basal segment. This has no consequences for the proximal characteristics of the shape of the cirral axis. One must keep in mind, however, that the most basal parts of the curvature and torsion curves may be missing.

There appears to be a striking similarity between the figures for $\kappa$ and $\tau$ for hyper- and depolarizing voltage steps. The pattern described above emerged in all the data we analyzed (responses to de- and hyperpolarizing voltage steps of 10 and 20 mV in both F2 and F3 cirri), but for general conclusions we feel still more data should be analyzed. The development of curvature in a tangential plane before twisting or bending perpendicular to that plane might point to a common mechanism, working both during DCA and HCA.

During DCA, bending occurs more proximally than during HCA (cf. Figs. 12 and 13. This explains the apparent contradiction between the width of the basal cones and the volume covered by the whole cirrus, as judged by the reconstructions (Figs. 4–7). During HCA, the basal segment describes a narrow cone, but its upright position (small inclination, Fig. 10 *b*, and Sugino and Machemer, 1987) allows the cirrus to bend freely and move on a wide trajectory. During DCA, the basal segment describes a much wider cone, which is inclined so that it almost lies on its side against the cell surface. This leaves the distal parts less freedom of movement; as a result, the beating cirrus covers a restricted volume, as demonstrated in Figs. 4 and 5.

We thank Dr. F. Bretschneider, Dipl. Biol. M. Weskamp, and Dipl. Inf. J. Pernberg for their help and stimulating discussions.
This work was supported by the Deutsche Forschungsgemeinschaft, Forschergruppe Konzell 3.

## APPENDIX

### Connection with model studies of axonemal bending

We have used the terms curvature and torsion in their general, "textbook" sense. In literature on ciliary and flagellar motion different descriptions for shape characteristics coexist. Sugino and Machemer (1988, 1990) interpret changes in planar bending as the rate at which sliding occurs between two adjacent doublets. As a consequence, 3D bending must involve transfer of sliding between different doublets in the axoneme. Planar bending in a small region of the axoneme may be described in terms of curvature, whereas rotation of the bending plane about the neutral axis is accompanied by torsion.

Hines and Blum (1983) start from a mathematically more rigorous description, defining curvature as a vectorial quantity $\mathbf{K} = (\kappa_x, \kappa_y, \kappa_z)$ resolved into three components of a coordinate system moving along the neutral axis of the axoneme. (**K** is capitalized here to distinguish it from the previously defined lower case $\kappa$ which is a scalar quantity.) Within this "body" coordinate system (not to be confused with the cell-based reference system used in this paper) the three components of **K** may be interpreted as follows: $\kappa_z$ is identical to the torsion $\tau$. The curvature $\kappa$ equals the magnitude of the vectorial addition of $\kappa_x$ and $\kappa_y$: $\kappa = \sqrt{\kappa_x^2 + \kappa_y^2}$. As stated by these authors, the direction of the $x$ axis may be chosen freely, for instance to align with a structural feature.

In its classical sense, as used in this paper, curvature quantifies bending in the direction of **N**, the binormal vector. When the $x$ and $y$ axes in the body coordinate system are known, $\kappa_x$ and $\kappa_y$ may be determined by resolving the vector along **N** with size $\kappa$ into two components along these coordinate axes.

For a meaningful choice of the direction of the "body" $x$ axis, additional information about the internal structure of the axoneme is required. In our analysis, only the "neutral" axis of the axoneme has been considered, and the occurrence of torsion does not allow any conclusions as to whether the axoneme itself is twisted (Holwill et al., 1979). If we assume that the internal structure of the axoneme is not twisted (Hines and Blum, 1984, 1985), the components $\kappa_x$ and $\kappa_y$ may be calculated. The assumption of absence of any net internal torsion requires the body coordinate system to rotate with exactly the amount of torsion $\tau$, that was calculated above.

With torsion $\tau(t, s)$ present, the rotation angle becomes:

$$\delta(t, s) = \int_0^s \tau(t, l)\, dl$$

integrated along the cirral axis. $\kappa_x$ and $\kappa_y$ are calculated as:

$$\kappa_x(t, s) = \kappa(t, s)\cos[\delta(t, s) + \delta_0(t)]$$

$$\kappa_y(t, s) = \kappa(t, s)\sin[\delta(t, s) + \delta_0(t)]$$

in which $\delta_0(t)$ stands for an initial direction of the body $x$ axis, at the cirral base.

In Figs. 14 and 15 the body $x$ axis is aligned at the base of the axoneme with the cell-based reference axis (Fig. 3). The initial angle $\delta_0(t)$ has been

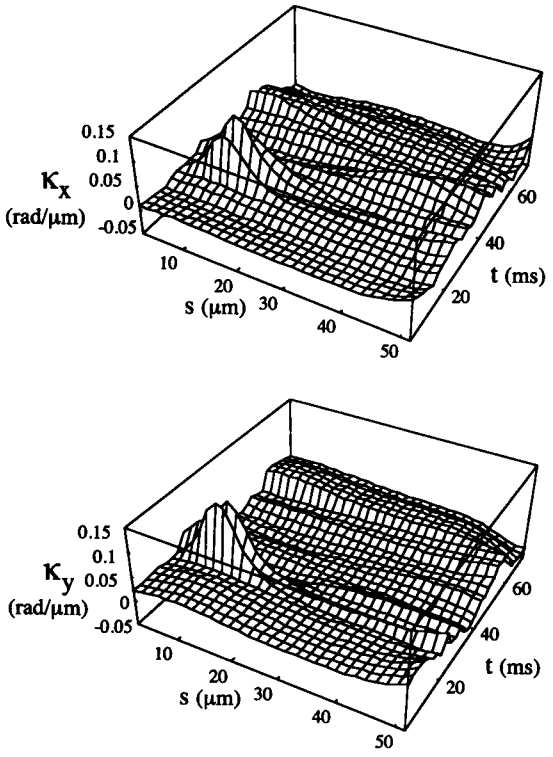


DCA

FIGURE 14 Curvature of DCA cycle calculated in Fig. 12 resolved into "body" $x$ and $y$ coordinates ($\kappa_x$ and $\kappa_y$), in absence of net internal torsion. At the base of the axoneme, the $x$ and $y$ axes coincide with the cell-based reference system (Fig. 3).

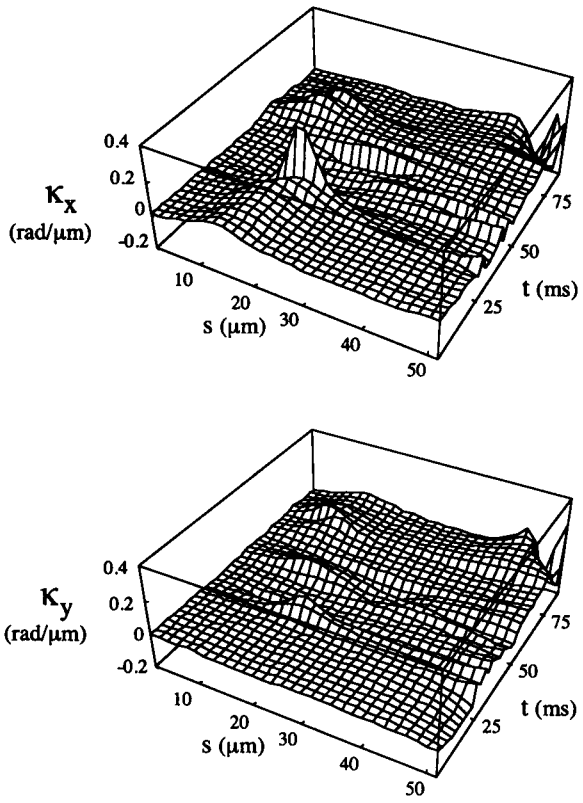


HCA

FIGURE 15 Curvature of HCA cycle calculated in Fig. 13 resolved into "body" $x$ and $y$ coordinates ($\kappa_x$ and $\kappa_y$), in absence of net internal torsion. At the base of the axoneme, the $x$ and $y$ axes coincide with the cell-based reference system (Fig. 3).

determined as follows: at the base ($s = 0$), a coordinate transformation was used to align the body $z$ axis with the tangential vector **T**. This was done by rotating the reference system about the smallest angle between the tangential vector **T** and the cell-based $z$ axis. Then $\delta_0(t)$ was taken as the angle between the binormal vector **N** and the transformed $x$ axis.

The similarities between Fig. 12 and both drawings in Fig. 14 indicate that twisting only has minor influence on the distribution of curvature over the $x$ and $y$ directions. The orientation of the reference frame at the cirral base determines the distribution of $\kappa$ into $\kappa_x$ and $\kappa_y$ in the body $xy$ plane. Although torsion is present in our reconstructions (Fig. 12), it is minimal in regions with significant curvature so that its influence on the shape of the cirral axis remains small.

Considering the responses to hyperpolarizing voltage steps, a similar result is found: the base angle constitutes the main factor influencing the distribution of curvature within the body $xy$ plane.

In the absence of internal torsion the direction of the curvature vector in the body $xy$ plane conveys information about which axonemal doublet may be involved in sliding. There are no marked differences in shape between $\kappa_x$ and $\kappa_y$ during both DCA and HCA. This may indicate that sliding transfer only takes place near the base of the axoneme. This emphasizes the importance of the basal region for the generation of 3D beating patterns. Although it is reasonable to assume that knowledge of the shape of the axoneme opens the possibility to assert which doublets slide by what amount, the generated forces still remain unknown. The significance of hydrodynamical loading for the shape of the beating cirrus needs more investigation.

## REFERENCES

Baba, S., and Y. Hiramoto. 1970. A quantitative analysis of ciliary movement by means of high-speed microcinematography. *J. Exp. Biol.* 52: 675–690.

Blake, J. 1972. A model for the micro-structure in ciliated organisms. *J. Fluid Mechanics.* 55:1–23.

Blake, J., and M. Sleigh. 1974. Mechanics of ciliary locomotion. *Biol. Rev. Camb. Philos. Soc.* 49:85–125.

Brokaw, C. 1971. Bend propagation by a sliding filament model for flagella. *J. Exp. Biol.* 55:289–304.

de Peyer, J., and H. Machemer. 1978. Are receptor-activated ciliary motor responses mediated through voltage or current? *Nature.* 276: 285–287.

de Peyer, J., and H. Machemer. 1982a. Electromechanical coupling in cilia. I. Effects of depolarizing voltage steps. *Cell Motil.* 2:483–496.

de Peyer, J., and H. Machemer. 1982b. Electromechanical coupling in cilia. II. Effects of hyperpolarizing voltage steps. *Cell Motil.* 2: 497–508.

Deitmer, J., H. Machemer, and B. Martinac. 1984. Motor control in three types of ciliary organelles in the ciliate *Stylonychia. J. Comp. Physiol. A,* 154:113–120.

Hines, M., and J. Blum. 1978. Bend propagation in flagella. I. Derivation of equations of motion and their simulation. *Biophys. J.* 23:41–57.

Hines, M., and J. Blum. 1983. Three-dimensional mechanics of eukaryotic flagella. *Biophys. J.* 41:67–79.

Hines, M., and J. Blum. 1984. On the contribution of moment-bearing links to bending and twisting in a three-dimensional sliding filament model. *Biophys. J.* 46:559–565.

Hines, M., and J. Blum. 1985. On the contribution of dynein-like activity to twisting in a three-dimensional sliding filament model. *Biophys. J.* 47:705–708.

Holwill, M., H. Cohen, and P. Satir. 1979. A sliding microtubule model incorporating axonemal twist and compatible with three-dimensional ciliary bending. *J. Exp. Biol.* 78:265–280.

Machemer, H., and J. de Peyer. 1982. Analysis of ciliary beating frequency under voltage clamp control of the membrane. *Cell Motil.* 1(Suppl.): 205–210.

Machemer, H., and J. Deitmer. 1987. From structure to behaviour: *Stylonychia* as a model system for cellular physiology. *In* Progress in Protistology, Vol. 2. J. Corliss and D. Patterson, editors. Biopress Limited, Bristol. 213–330.

Machemer, H., and K. Sugino. 1986. Parameters of the ciliary cycle under membrane voltage control. *Cell Motil. Cytoskeleton.* 6:89–95.

Mogami, Y., and H. Machemer. 1991. In vivo activation of cirral movement in *Stylonychia* by calcium. *J. Comp. Physiol.* 168:687–695.

Mogami, Y., J. Pernberg, and H. Machemer. 1992. Ciliary beating in three dimensions: steps of a quantitative description. *J. Math. Biol.* 30:215–249.

Oppenheim, A., and R. Schafer. 1975. Digital Signal Processing. Prentice-Hall International, New York.

Press, W., B. Flannery, S. Teukolsky, and W. Vetterling. 1989. Numerical Recipes in C: The Art of Scientific Computing. Cambridge University Press, Oxford.

Sleigh, M. 1968. Patterns of ciliary beating. *In* Aspects of Cell Motility, Vol. 22, Symposium of The Society for Experimental Biology, Academic Press, San Diego, CA, 131–150.

Sugino, K., and H. Machemer. 1987. Axial-view recording: an approach to assess the third dimension of the ciliary cycle. *J. Theor. Biol.* 125:67–82.

Sugino, K., and H. Machemer. 1988. The ciliary cycle during hyperpolarization-induced activity: an analysis of axonemal functional parameters. *Cell Motil. Cytoskeleton.* 11:275–290.

Sugino, K., and H. Machemer. 1990. Depolarization-controlled parameters of the ciliary cycle and axonemal function. *Cell Motil. Cytoskeleton.* 16:251–265.

Teunis, P., Bretschneider, F., and H. Machemer. 1992. Realtime 3D-tracking of fast moving microscopic objects. *J. Microsc.* 168:275–288.

Thomas, G., and R. Finney. 1992. Calculus and Analytic Geometry. Addison-Wesley Publishing Company, Redding, MA.

Wolf, R. 1989. A novel beam-splitting microscope tube for taking stereo-pairs with full resolution Nomarski or phase contrast technique, or with epifluorescence. *J. Microsc.* 153:181–186.

Woolley, D. 1981. A method for determining the three-dimensional form of active flagella, using two-colour darkground illumination. *J. Microsc.* 121:241–244.

Woolley, D., and I. Osborn. 1984. Three-dimensional geometry of motile hamster spermatozoa. *J. Cell Sci.* 67:159–170.